

Topologically nontrivial magnonic solitons

Mehrdad Elyasi,¹ Koji Sato,¹ and Gerrit E. W. Bauer^{2,3}

¹*Institute for Materials Research, Tohoku University, 980-8577 Sendai, Japan*

²*Zernike Institute for Advanced Materials, University of Groningen, The Netherlands*

³*Institute for Materials Research & AIMR & CSRN, Tohoku University, 980-8577 Sendai, Japan*

The intrinsic non-linearities of the spin dynamics in condensed matter systems give rise to a rich phenomenology that can be strongly affected by topology. Here we study formation of magnonic solitons in the topologically nontrivial bandgap of a spin lattice realization of the Haldane model, in both static and dynamic (Floquet) regimes. We consider nonlinearities caused by magnetic crystalline anisotropy and magnon-magnon interactions. We find soliton formation power thresholds as a function of anisotropy coefficient and interaction strength. We predict different classes of topological solitons for the same topological class of the underlying lattice and explain it in terms of a transition from a topologically nontrivial mass to a trivial one. Our findings imply that a soliton can phase-separate, containing boundaries between topologically trivial and non-trivial phases, which is associated with a vanishing spin wave gap.

I. INTRODUCTION

In physics, topological equivalence classes refer to Hamiltonians with energy gaps that with smooth changes in parameter space do not become gapless unless a quantum phase transition occurs. The robustness with respect to perturbations^{1,2}, as well as the potential for quantum computation³ made topology an important subfield of modern condensed matter physics. Topology manifests itself, for instance, in the quantum Hall effects⁴⁻¹⁰, 3D topological band insulators^{1,2,11,12}, and quantum spin liquids¹³⁻¹⁶. Chiral, or in the case of the quantum spin Hall effect, helical⁶ edge modes are caused by bands with nontrivial global phases derived from the topology of the bulk material. Topology affects the wave functions of electrons^{2,7,17}, photons¹⁸, phonons¹⁹, magnons²⁰, and quasi-particles such as Majorana fermions²¹.

In continuous media, the Damon-Eshbach (DE) surface modes in ferromagnetic films are chiral^{22,23}, but not proven yet to be topological. Nevertheless, the topology (i.e. the Berry curvature) of magnon bands in perpendicular magnetized films has been revealed in phenomena such as the magnon Hall effect and the rotation of wave packets at the edges^{24,25}. Motivated by the established topological band theory², topological chiral magnonic edge modes in gapped magnonic crystals have attracted attention. Spin wave dispersions in ferromagnets are governed by both dipolar and exchange interactions. In a lattice with nonuniform equilibrium magnetization, the former can break the inversion and time reversal symmetry, leading to bands with nonzero Chern number. This implies emergence of chiral edge modes at the boundary of the lattice with vacuum (or a lattice with different topology)²⁰. The exchange interaction can also be utilized to design magnonic analogues of static or Floquet-type²⁶⁻²⁸ Haldane⁵ spin lattice models²⁹⁻³³. The periodic Floquet variable can be the time or a spatial coordinate. In 2D spatial lattices, e.g., time²⁸ as well as the third spatial coordinate normal to the 2D plane³⁴ have been employed as the Floquet dimension.

In the case of Fermions, the chiral (or helical) edge modes can be populated at all temperatures when the chemical potential falls into a non-trivial band gap. Magnons and other Bosonic edge states, on the other hand, tend to be empty at low temperatures, which makes experimental observation challenging. This motivated proposals to utilize non-linear interactions that can drive edge mode instabilities³⁵ or lead to self-localized wave packets with a sense of chirality inherited from the original edge modes³⁶⁻³⁸.

Solitons are shape-preserving, self-localized modes in dispersive media. In magnets, solitonic textures such as domain walls, vortices and skyrmions that exist in equilibrium can be topologically protected³⁹. They also emerge as robust excited states, in which nonlinear interactions compensate the wave packet dispersion. The latter type of solitons have been explored theoretically and experimentally in both continuous and discrete systems such as Bose-Einstein condensates of cold atoms in optical potentials⁴⁰⁻⁴³ as well as light in fibres and photonic crystals^{36,37,44-47}. Solitons in thin magnetic films can be excited by microwaves^{23,48-50}. Subsequently, magnonic solitons have been generated in nano-contacts by spin-transfer^{51,52} and spin-orbit torques⁵³. When the spin current is injected locally into an in-plane magnetized film above a certain threshold, the exchange dispersion is compensated by a focusing nonlinearity, and a self-localized non-propagating spin-wave mode emerges at a frequency below the predictions of linear theory⁵⁴, which is referred to as “spin wave bullet”. Droplets of magnon condensates as generated by parametric pumping can be interpreted as solitons as well⁵⁵⁻⁵⁷.

Here we show that the non-linearities generated by crystalline magnetic anisotropy and magnon-magnon interactions can generate magnonic solitons that show signatures of the topology of the underlying spin wave band structure of magnonic crystals with nontrivial band gaps. We search for solitons in the bulk of static and time-periodic (Floquet) magnonic equivalents of the Haldane model, i.e. a hexagonal lattice with C_{6v} point group symmetry, but broken time-reversal symmetry⁵. We chose

the Haldane model as a minimal but generic model with a single band gap but nontrivial topology. The results can be extended to other lattices with band gaps of similar topology. We attribute the different solitons phases in parameter space to distinct topologies, even mixed topologies. For the latter case we predict the existence of interfaces between topologically trivial and non-trivial highly excited phases.

The paper is organized as follows. Section II addresses solitons in the topologically nontrivial band gap of a static magnonic Haldane model. Section II A describes the model and the numerical method used to find solitons. In section II B we show calculated soliton phase diagrams, and explain them in Sec. II C. In section III we focus on the soliton phase diagram in the Floquet equivalent of the Haldane model. Finally, in Sec. IV, we evaluate the experimental feasibility and propose two methods to test the findings of this paper.

II. SOLITONS IN THE STATIC MAGNOMIC HALDANE MODEL

A. Model

The equivalent of the Haldane model⁵ for magnons can be derived from the Hamiltonian^{31,32},

$$H_S = \sum_{\langle i,j \rangle} J \vec{S}_i \cdot \vec{S}_j + \sum_{\langle\langle i,j \rangle\rangle} D v_{ij} \hat{z} \cdot \vec{S}_i \times \vec{S}_j \quad (1)$$

on a 2D hexagonal lattice of spins \vec{S}_i with Heisenberg nearest neighbor exchange interaction J and Dzyaloshinskii-Moriya interaction D (DMI)^{58,59}. The lattice sites i and j in the second term of the right-hand side are next-nearest neighbors (NNN), $v_{ij} = +(-)1$ on the upward (downward) pointing NNN triangle, as sketched in Fig. 1(a). This Hamiltonian can support edge modes in the gap because the nontrivial global phase or Berry curvature leads to bands with nonzero Chern numbers (± 1 , depending on the sign of D)⁶⁰. Each spin quantum number S is defined by $\vec{S}^2 = \hbar^2 S(S+1)$. Raising and lowering operators read $S^\pm = S_x \pm iS_y$, respectively. According to the Holstein-Primakoff (HP) transformation $S^+ = \sqrt{2S}a^\dagger(1 - a^\dagger a/(2S))^\frac{1}{2}$, $S^- = \sqrt{2S}(1 - a^\dagger a/(2S))^\frac{1}{2}a$ and $S_z = S - a^\dagger a$, in terms of boson creation (a^\dagger) and annihilation operators (a). When the number of magnons $\sum_i a_i^\dagger a_i$ is a small fraction of NS , where N is the number of spins, we can expand the square roots as $S^+ \approx \sqrt{2S}a^\dagger$ and $S^- \approx \sqrt{2S}a$. However, the “participation” $\langle \Psi_s | a_i^\dagger a_i | \Psi_s \rangle$ of a localized soliton mode $|\Psi_s\rangle$ can become of the order of S , even when the total magnon number is small. $(1 - a^\dagger a/(2S))^\frac{1}{2}$ can then not be approximated by unity, i.e., nonlinear terms in the Hamiltonian must be considered.

Other non-linearities can be added to the Haldane Hamiltonian Eq. (1), such as an on-site magnetic

anisotropy. Here we consider uniaxial perpendicular magnetic anisotropy $\sum_i K S_{z,i}^2$. When K is negative (positive), the anisotropy is of the easy-axis (easy-plane) type. The Zeeman energy for a magnetic field $\vec{H} = (0, 0, H_{ext,z})$ is $H_Z = g\mu_B \sum_i H_{ext,z} S_{z,i} = g\mu_B \sum_i H_{ext,z} S - H_{ext,z} a_i^\dagger a_i$, where g is the g-factor, μ_B is the Bohr magneton. When the ground state magnetization is aligned $\parallel \hat{z}$, H_Z rigidly shifts the entire spin wave dispersion. This is always the case for perpendicular crystalline anisotropy, while $H_{ext,z}$ should be sufficiently large when the anisotropy is easy-plane. The spin-orbit interaction is an essential ingredient of our theory by generating a gap in the magnon spectrum. But in practice is rather weak. We find for realistic values of the parameter D that the canting of spins relative to the quantization axis \hat{z} is so small that it can be safely disregarded, e.g., in discussing the magnetic field dependence of the computed results. Magneto-dipolar interactions are disregarded under the assumption that magnons with wave lengths larger than the exchange length do not play a dominant role.

Consolidating the above: we work with the Hamiltonian

$$\begin{aligned} H_T = & -JS \sum_{\langle i,j \rangle} (a_i^\dagger a_j + H.c.) + \\ & (3JS - 2KS - g\mu_B H_{ext,z}) \sum_i a_i^\dagger a_i \\ & - DS \sum_{\langle\langle i,j \rangle\rangle} (iv_{ij} a_i^\dagger a_j + H.c.) + H_{NL}, \end{aligned} \quad (2)$$

with non-linearities to the fourth order in field operators :

$$\begin{aligned} H_{NL} = & \frac{J}{4} \sum_{\langle i,j \rangle} \left[(a_i n_i a_j^\dagger + a_i n_j a_j^\dagger + a_i^\dagger n_i a_j + a_i^\dagger n_j a_j) \right. \\ & \left. - 2a_i a_j^\dagger - n_i n_j \right] - \frac{D}{4} \sum_{\langle\langle i,j \rangle\rangle} iv_{ij} \left[(a_i^\dagger n_i a_j + a_i^\dagger n_j a_j) \right. \\ & \left. - (a_i n_i a_j^\dagger + a_i n_j a_j^\dagger) - 2a_i a_j^\dagger \right] + \sum_i K(n_i)^2, \end{aligned} \quad (3)$$

where the occupation number $n_i = a_i^\dagger a_i$. The choice $-2KS = g\mu_B H_{ext,z}$ takes care of the alignment of the spins as well as the band edge for all parameters which helps to interpret the calculated phase diagrams. (With the exception of the term $n_i n_j$) the operators $n_{i(j)}$ appear in a “sandwiched” form such as $a_i n_i a_j^\dagger$. We refer to the non-linearities generated by the anisotropy K as “self-Kerr effect”, since it generates a frequency shift proportional to the number operator (that should not be confused with the magneto-optical Kerr effect).

Rather than attempting to diagonalize this Hamiltonian, we iteratively search for self-consistent soliton solutions. We start with a localized initial trial wave function (WF) $|\Psi_0\rangle$ with density $\langle \Psi_0 | n_i | \Psi_0 \rangle = P_0 > 0$ for a site $i = 0$ deep in the bulk and zero otherwise. We

keep P_0 constant during subsequent iterations by requiring $\sum_i \langle \Psi_m | n_i | \Psi_m \rangle = \sum_i P_i^{(m)} = P_0$, where m is the iteration step. This H_{NL} can be rewritten in terms of real space spinors $\psi_i = (a_i, a_i^\dagger)^T$ to become matrices $\mathbf{H}_T^{(m)}$ with dimension $2N_x \times N_y$, where N_x (N_y) is the number of sites in the x (y) axis:

$$\mathbf{H}_T^{(m)} = \sum_{i,j} \psi_j^\dagger \mathcal{H}(P_i^{(m-1)}, P_j^{(m-1)}) \psi_i. \quad (4)$$

$\mathcal{H}(P_i^{(m-1)})$ depends on $|\Psi_{m-1}\rangle$ by the nonlinear (non-bilinear) terms in H_{NL} . $\mathbf{H}_T^{(m)}$ is diagonalized and $|\Psi_m\rangle$ is chosen to be the eigenstate with the highest overlap $|\langle \Psi_m | \Psi_{m-1} \rangle|$. Self-consistency is reached when the overlap approaches unity by a certain criterion for a solution with $\forall_i P_i < 2S$. Solitons are self-localized, dispersionless wavepackets that exist in the energy gaps of band structures. The Haldane model has one finite band gap that splits the density of states but also a finite spectral width with zero density of states at high and low energies (semi-infinite gaps) (see Fig. 1(b)). Solitons can exist in the three gaps, but they can be topologically relevant only in the internal band gap that can support edge modes. We limit our search to solutions with frequencies in the bandgap and thereby discard possible solutions outside the band edges.

This iterative method sometimes fails to converge to a single solution. We can overcome that problem by implementing an auxiliary temporal periodicity as described in Appendix A.

B. Results

Figure 1(b) shows the band structure of the linearized spin Hamiltonian Eq. (1) for an infinitely long quasi-1D ribbon that is 80 lattice sites wide with staggered (zigzag) free (open) boundary condition at the edges. It hosts a topologically nontrivial band gap of $6\sqrt{3}DS$ (see Sec. II C) with chiral edge modes. We assume $S = 10$, $J = 0.1$ and $D = 0.01$ in all of the calculations in this paper, unless otherwise stated. We carry out the bulk soliton search in the finite gap of a lattice with $N_x = 40$ and $N_y = 80$ and free boundary condition in x and y direction, with armchair and staggered edges, respectively. We first focus on non-linearities caused by the anisotropy and non-interacting magnons, i.e. when $\forall_i \langle \Psi_s | a_i^\dagger a_i | \Psi_s \rangle \ll S$, and discuss the magnon-magnon interaction below. The results of the soliton search can be summarized by a phase diagram as a function of intensity P_0 and anisotropy K . The energy of a converged solution E_s is indicated by the color code of the side bar in Fig. 1(c). Mathematically, the assumption of non-interacting magnons remains valid for other parameter regimes by scaling S up with coefficient $\mathcal{C} > 1$, while scaling down J and D by $1/\mathcal{C}$.

The threshold $P_0 = P_{c,1}$, marked by green-dotted lines in Fig. 1(c) is the intensity above which we find self-

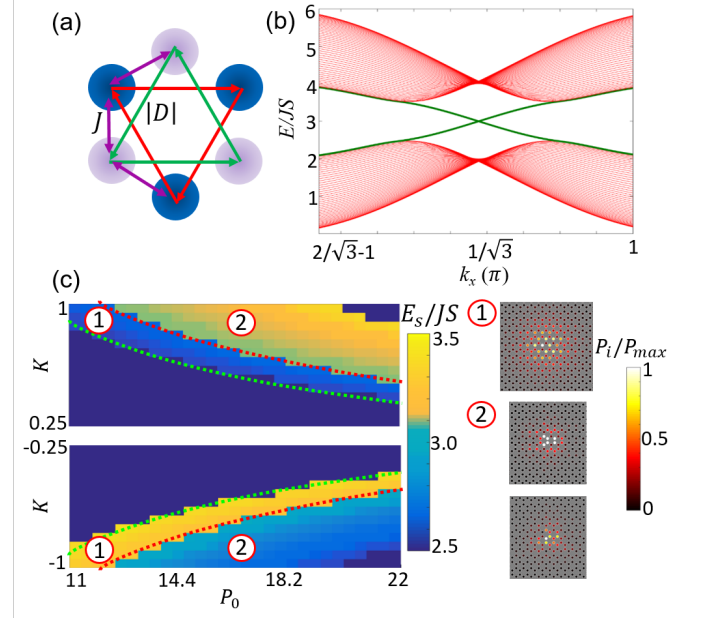


FIG. 1. (a) Schematics of the lattice, the Heisenberg exchange interactions (purple lines), and the NNN DMI interactions (green ($v_{ij} = 1$) and red ($v_{ij} = -1$) lines). (b) The band-structure of a 80 sites wide, quasi-1D ribbon with $J = 0.1$, $D = 0.01$, $K = 0$, and $S = 10$. The edge states (green lines in the gap) merge with the band edges for large wave numbers. (c) Soliton phase diagram in the space of anisotropy constant K and integrated intensity P_0 . In the dark-blue area no solution was found. The color map indicates the energy E_s of the calculated solitons. 1 and 2 label the distinct parts of the phase diagram. The right panels display representative soliton density distributions found in 1 (the top one) and 2 (the two bottom ones, which are basically the same for both signs of K). Green and red dashed lines mark the thresholds $P_{c,1}$ and $P_{c,2}$, respectively, as detailed in the text. In the color code of the right panels, $P_{max} \lesssim 1.5S$ is the peak value of $P_i = \langle \Psi_s | n_i | \Psi_s \rangle$.

stabilized soliton solutions. The solitons in the first region just above $P_{c,1}$ have energies close to the band edges. Their amplitudes (or “wave functions”, WF, intensity) are spatially relatively extended, as seen in the right panel of Fig. 1(c). We note the large differences for positive and negative anisotropy: The energies of the solitons for $K > 0$ ($K < 0$) are closer to the lower (upper) band edge for smaller P_0 but move to the upper (lower) band edge with increasing P_0 . For $K < 0$ ($K > 0$), the non-linearity tends to localize (delocalize) the WFs; a soliton mode exists by compensation of nonlinearity and diffraction, so the effective mass at the band edge must be positive (negative), which is the case at the upper (lower) edge. $K < 0$ ($K > 0$) can be referred to as focusing (defocussing) non-linearities, respectively. The focusing nonlinearity can lead to solitons in both continuous and discrete media, while the defocussing nonlinearity supports solitons only in lattices with gaps.⁴³ This difference becomes important when non-local magnon-magnon

interactions are taken into account (see below).

A second threshold $P_0 = P_{c,2}$ as indicated by the red-dash line in Fig. 1(c) marks a very different phase boundary; there is a sharp change in energy and is also observed for the equivalent Floquet lattice, see the discussion below and in Sec. III.

Above a third threshold (not shown) the iterative solution scheme fails to converge, but oscillates between two (or more) states. This means that the eigenfunction of the (mean-field) nonlinear potential induced by one soliton is a different soliton with different energy, indicating “breathing”. This situation is an artifact of the choice of the initial condition. We implement a numerical method based on an auxiliary time periodic potential as described in Appendix A in order to converge unphysical breathing modes to steady state soliton solutions.

The results in Figs. 1(c) hold when (for fixed S/J and K) S is sufficiently large and the magnon interaction is small. In the following we demonstrate how the higher order terms in the HP expansion proportional to J and D in Eq. (3) modify the soliton phase diagram. The numerical procedure is the same as before. Figure 2 illustrates a first phase boundary at threshold $P'_{c,1}$ for solitons as those in region 1(2) of Fig. 1(c) for $K > 0$ ($K < 0$), respectively. For $K > 0$, a phase boundary at $P'_{c,2}$ (the red dashed line in Fig. 2) similar to the one at $P_{c,2}$ in Fig. 1(c) exists. Region 1'(2') in Fig. 2 is similar to region 1(2). When (sufficiently strong) magnon-magnon interactions are included, i.e. the terms proportional to J and D in Eq. (3), the phase boundary marking topological distinct phases exists only when $K > 0$ (see Fig. 2), because these interactions are of the focusing type in continuous magnetic media^{23,48}. They assist the local Kerr nonlinearity for $K < 0$ but oppose it when $K > 0$, preventing formation of extended solitons in region 1' to form for $K < 0$. Interaction also shifts the onset of soliton formation $P_{c,1}$ to lower P_0 for the same $K < 0$, while the topological change threshold moves to higher P_0 , i.e. $P'_{c,2} > P_{c,2}$ for $K > 0$.

A scaling that extends the parameter space for which the present calculations are valid, corresponds to keeping S , K , and J/D constant, while scaling down J . This decreases P_{max} and therefore P_{max}/S . Approximating the envelope cross sections of solitons of region 1 (1') by solutions of an effective 1D nonlinear Schrödinger equation^{61,62}, we deduce that P_{max} is reduced by a factor 10 when J/S is reduced by a factor 100. Therefore, for $S = 1$, $J = 0.01$ and $D = 0.001$, the phase diagrams as Fig. 1(c) and Fig. 2 hold for ~ 10 times smaller P_0 , ~ 100 times smaller energies, while P_{max}/S remains the same. We therefore can extend our arguments to small spin systems when the exchange interaction is small enough.

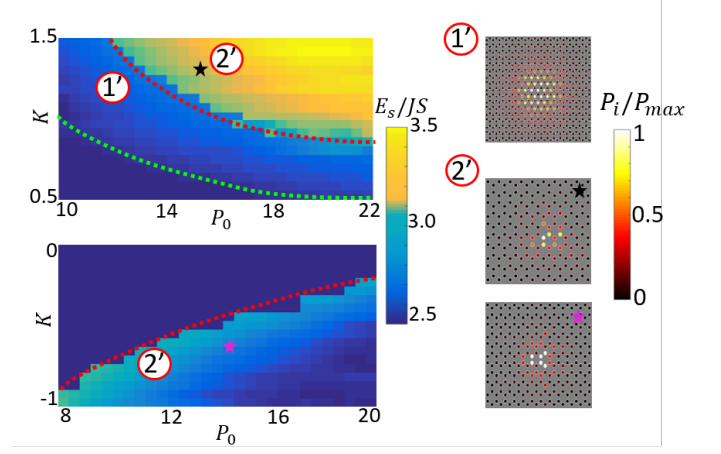


FIG. 2. The bulk soliton formation phase diagram for interacting magnons. The intensity distribution of a soliton in region 1' as well as two examples (marked by black and purple stars) in region 2' are shown. The green (red) dashed line indicates $P'_{c,1}$ ($P'_{c,2}$).

C. Discussion

We now compare our results for local excitations in a wire to that of a homogeneous excitation of the bulk system, following an analysis of the Su-Schrieffer-Heeger (SSH) model⁶³, i.e. spinless electrons on a one-dimensional lattice with staggered hopping amplitudes, for which an anharmonicity in the phonon amplitude causes a phase transition from a topologically trivial to nontrivial phase⁶⁴.

We can express the Haldane model in reciprocal space $H_T = \sum_{\vec{k}} \psi_{\vec{k}}^\dagger \mathcal{H}_{\vec{k}} \psi_{\vec{k}}$, where the spinor $\psi_{\vec{k}} = (b_{\vec{k}}, c_{\vec{k}})^T$ is written in terms of the electron annihilation operators $b_{\vec{k}}$ and $c_{\vec{k}}$ on the two sublattices. We can map the linearized magnetic Hamiltonian Eq. (2) to this form by

$$\mathcal{H}_{\vec{k}}(\vec{k}) = q_0 I + \mathbf{q}(\vec{k}) \cdot \vec{\sigma}, \quad (5)$$

where $q_0 = 3JS$, I is the 2×2 unit matrix, $\vec{\sigma} = [\sigma_x, \sigma_y, \sigma_z]^T$ is the vector of Pauli matrices,

$$\mathbf{q}(\vec{k}) = \begin{pmatrix} -JS \sum_i \cos(\vec{k} \cdot \vec{\lambda}_{NN,i}) \\ -JS \sum_i \sin(\vec{k} \cdot \vec{\lambda}_{NN,i}) \\ -2DS \sum_i \sin(\vec{k} \cdot \vec{\lambda}_{NNN,i}) \end{pmatrix}, \quad (6)$$

and $\vec{\lambda}_{NN,i}$ ($\vec{\lambda}_{NNN,i}$) is one of the three (i.e. $i = 1, 2, 3$) lattice vectors to the NN (NNN) sites. The energies $\mathcal{E}(\vec{k})$ and wave functions $|\Psi_{\vec{k}}\rangle$ for the two bands are

$$\mathcal{E}(\vec{k}) = q_0 \pm \sqrt{\mathbf{q} \cdot \mathbf{q}}, \quad (7)$$

$$|\Psi_{\vec{k}}\rangle = \frac{1}{\sqrt{2}} \begin{pmatrix} \sqrt{1 \pm \frac{q_z(\vec{k})}{\sqrt{\mathbf{q} \cdot \mathbf{q}}}} \\ \mp \exp\left(-i \tan^{-1} \frac{q_y(\vec{k})}{q_x(\vec{k})}\right) \sqrt{1 \mp \frac{q_z(\vec{k})}{\sqrt{\mathbf{q} \cdot \mathbf{q}}}} \end{pmatrix}. \quad (8)$$

The anisotropy is now represented by a 2×2 nonlinear Hamiltonian \mathcal{H}_{NL} which is diagonal in the mean-field approximation with components $[\mathcal{H}_{\text{NL}}(\vec{k})]_{1,1} = KP_u \langle \Psi_{\vec{k}} | b_{\vec{k}}^\dagger b_{\vec{k}} | \Psi_{\vec{k}} \rangle$ and $[\mathcal{H}_{\text{NL}}(\vec{k})]_{2,2} = KP_u \langle \Psi_{\vec{k}} | c_{\vec{k}}^\dagger c_{\vec{k}} | \Psi_{\vec{k}} \rangle$, where P_u is the density per unit cell of the homogeneously excited system. Eqs. (7), (8), and \mathcal{H}_{NL} define a self-consistent problem that has to be solved numerically for each \vec{k} . At the Dirac points $\vec{k}_1 = [4\pi/3, 0]$ and $\vec{k}_2 = [2\pi/3, 2\pi/\sqrt{3}]$ (a similar discussion applies to the four other Dirac points), at which the gap opens and closes, $\mathbf{q}(\vec{k}_1) = 3\sqrt{3}DS\hat{\mathbf{z}}$ and $\mathbf{q}(\vec{k}_2) = -3\sqrt{3}DS\hat{\mathbf{z}}$. Therefore, $\mathcal{H}_{\text{NL}} = KP_u(I \pm \sigma_z)/2$, plus (minus) holding when only the upper (lower) bands contribute, which is the case when K is negative (positive). The \mathcal{H}_{NL} therefore simply adds a mass coefficient $\mathcal{M} = \pm KP_u/2$ to q_z in the unperturbed Hamiltonian. It can be shown that the Chern number is ± 1 if $-6\sqrt{3}DS < KP_u < 6\sqrt{3}DS$ and vanishes otherwise. Therefore, by increasing P_u for any sign of K , a transition from topologically nontrivial to trivial phase occurs at a critical $P_{u,c} = 6\sqrt{3}DS/|K|$. Magnons with focusing (defocusing) nonlinearity belong to a band with positive (negative) effective mass, i.e. upper (lower) band, just as in insulators with trivial bandgaps⁶⁵. Therefore, the trivial mass term with coefficient \mathcal{M} as discussed above stems only from one of the bands, depending on the sign of K .

When the mass in the core of the soliton changes from nontrivial to trivial, the soliton mode should be exponentially localized in the area where the trivial and nontrivial topology meet, i.e. at the edges^{1,2}. This is indeed evident from the spatial WF of solitons of regions 1 (1') and 2 (2') (see Fig. 1(c) and Fig. 2): For the same P_0 , the energy of the more localized soliton is higher (lower) for positive (negative) K , simply because the self-Kerr nonlinearity $\sum_i K(n_i)^2$ in Eq. (3) indicates that $|K| \times N_{s,1} \times (P_0/N_{s,1})^2 > |K| \times N_{s,2} \times (P_0/N_{s,2})^2$ and $N_{s,1} > N_{s,2}$, where $N_{s,1}$ ($N_{s,2}$) is the number of sites with relatively large participation in the soliton WF of region 1 or 1' (2 or 2'). The abrupt change of the boundary conditions causes a jump in the formation energies by the non-trivial boundary conditions. In a homogeneously excited system in which the Chern number is well defined, we find the transition at similar values of P_{max} (see Fig. 3), which is another indication that the soliton core is bulk-like.

Figure 3 shows the peak intensity $P_{\text{max}} = \max \langle \Psi_s | a_i^\dagger a_i | \Psi_s \rangle$ as a function of P_0 for different values of K corresponding to the solitons of Fig. 1(c) and compares it with the $P_{u,c}(K)$ for the bulk systems represented by horizontal lines. When the integrated intensity of the soliton P_0 increases to $P_{\text{max}} = P_{u,c}$ a phase change is expected. Indeed, at those powers P_{max} jumps to a

higher level. In Fig. 3, $P_{\text{max}} < P_{u,c}$ when $P_0 < P_{c,2}$, but $P_{\text{max}} > P_{u,c}$ for $P_0 > P_{c,2}$. We therefore conclude we can understand the phase boundary $P_{c,2}$ in terms of the bulk-like mechanism in the soliton core. A similar relation for the bulk systems can be obtained for the interacting system (not shown) with phase change that occurs at $P'_{c,2}$ of Fig. 2. Therefore, in regions 1 and 1', the maximum soliton WF intensity (and therefore that at each site) is less than $P_{u,c}$, which means that the topology remains nontrivial and the entire lattice has the same Chern number ($C = \pm 1$). In regions 2 and 2', the soliton WF intensity at the center is larger than $P_{u,c}$, hence the topology of the central part of the soliton (trivial, $C = 0$) and the rest of the lattice (nontrivial, $C = \pm 1$) is different.

If our interpretation is correct, edge modes around the core of the solitons in region 2 (2') should generate a finite local density of state (LDOS), which for a site i reads⁶⁶

$$\rho_i(E) = \frac{-1}{\pi} \sum_n |\Psi'_n(i)|^2 \text{Im} \frac{1}{E - E_n + i\epsilon}, \quad (9)$$

where the sum is over all self-consistent eigensolutions $\Psi'_n(i)$, E_n of H_T (see Eq. (2)), and ϵ is a small broadening. Figure 4(a) shows $\rho_i(E)$ for a soliton in region 1 (left) and region 2 (right) of Fig. 1(c), for E inside the bandgap. The dominant peaks in $\rho_i(E)$ agree with the soliton energies that are indicated by black dashed lines. The soliton of region 2 is distinguished by additional two relatively large peaks in the band gap that do not exist for the solitons of type 1. We define $\tilde{\rho}_i(E) = 0$ for $E_s - \epsilon < E < E_s + \epsilon$ and $\tilde{\rho}_i(E) = \rho_i(E)$ otherwise, where $\epsilon = JS/1000$; in other words we blend out the LDOS of the soliton in order to enhance additional features. We then define $\rho_{M,i}$ as the maximum value of $\tilde{\rho}_i(E)$ as a function of E at each site i . Figure 4(b) shows $\rho_{M,i}$ of the solitons in regions 1 and 2 as in Fig. 4(a). Ignoring the sample boundaries, the excess LDOS is large in the bulk (defining the soliton core) for the soliton phase 2 (but none is left in 1). Figure 4(b) is strong evidence that the soliton of region 2 (2') is surrounded by edge modes, which supports the conjecture of a boundary between two regions with different topology. In other words, the “mass transition” from nontrivial to trivial, i.e. the gap opening by a trivial mass term $q_z = \mathcal{M}$ in the Hamiltonian is $\mathcal{M}\sigma_z$ or nontrivial one when q_z is as in Eq. (6), generates edge states in the bulk around the soliton core of type 2 (2'). We note that computational limitations force us to consider only small solitons, so Fig. 4(b) does not resolve the ring-like LDOS expected for edge states.

We conclude that the soliton WF has a nonzero intensity in two regions with different topology. Figures 5(a-b) illustrate this scenario. Figure 5(a) is a sketch of the two possible situations, where the non-trivial situation is the right panel and the interesting interface is indicated by the red dotted line. Figure 5(b) shows the spin wave band structure for a topologically trivial and a nontrivial Haldane model with the same gap, including the calculated Berry curvature $\vec{\Omega}(\vec{k}) = \Omega(\vec{k}) \hat{\mathbf{z}} =$

$\nabla_{\vec{k}} \times \langle \Psi(\vec{k}) | i \nabla_{\vec{k}} | \Psi(\vec{k}) \rangle$ ^{60,67}, while $C = \int_{\text{BZ}} dk^2 \Omega(\vec{k}) / (2\pi)$, where BZ stands for the first Brillouin zone. These band structures are global and cannot simply be assigned to a small number of lattice sites such as the soliton core. Indeed, assigning non-local properties such as a Chern number to a small number of lattice sites such as the soliton core is not completely rigorous, but as our discussion above indicates it is still a useful heuristic instrument.

Appendix B analyzes the phase texture of the soliton WF's in support of the above discussion.

III. SOLITONS IN THE FLOQUET MAGNONIC HALDANE MODEL

We now turn to the Floquet problem of the Haldane model with a periodic potential in time. Solitons can exist in Floquet photonic topological insulators, i.e. lattices of helical waveguides with on-site Kerr nonlinearity ($\sim n_i^2$ in Eq. (3)), in which the pitch of the helix is the (spatial) Floquet period. Static bulk and propagating edge solitons have been predicted^{36–38}. Here we focus on the magnonic Haldane model with a time-periodic perturbation³³:

$$H_F = J \sum_{\langle i,j \rangle} S_i^z S_j^z + \frac{J}{2} \sum_{\langle i,j \rangle} [S_i^+ S_j^- e^{iA_{ij}(t)} + h.c.], \quad (10)$$

where A_{ij} is the Aharonov-Casher phase⁶⁸ accumulated upon hopping between nearest neighbors. It

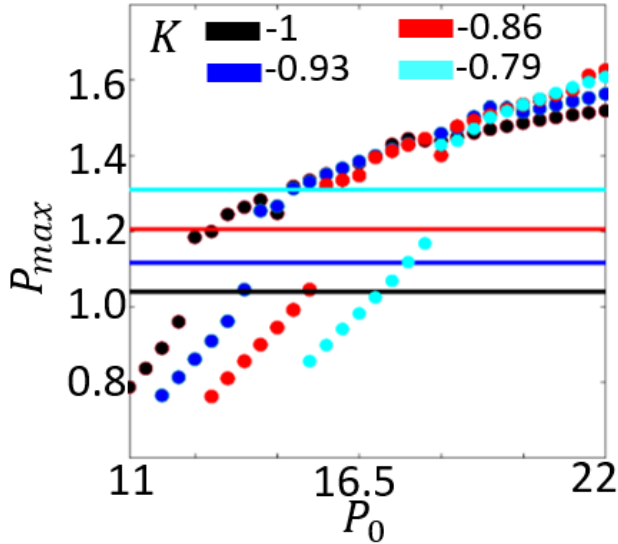


FIG. 3. Peak intensity P_{max} for soliton formation calculated for four different values of the anisotropy parameter K as in Fig. 1(c). The horizontal lines represent $P_{u,c}$, for the same K 's of homogeneously excited system, which agree with the jumps in P_{max} , indicating the distinct topology between regions 1 and 2.

can be generated by elliptically polarized light propagating normal to the lattice plane. The Hamiltonian in Eq. (10) oscillates with period T of the light field. The non-topological Heisenberg Hamiltonian ($A_{ij} = 0$) can thus be driven to generate a topologically non-trivial band structure. In other words, in $\mathcal{T} \exp \left(-i \int_0^T H_F(t) dt \right) |\Psi\rangle = \exp(-i\alpha T) |\Psi\rangle$, where \mathcal{T} is the time ordering operator and $|\Psi\rangle$ is the Floquet eigenstate, the band structure that underlies the quasi-frequency α can be topologically nontrivial, even when the band structure for the static part of H_F is trivial²⁸.

We choose a periodic potential that gives rise to the Floquet equivalent of the static Haldane model considered in Fig. 1 (see Appendix C for details of the Floquet lattice³³), which can be treated by the soliton search method described in Appendix A³⁶. Figure 6 shows the soliton quasi-energies α for $K = -1$ without magnon-magnon interactions. Regions 1 and 2 of the static case (see Figs. 1(c)) also exist for the Floquet problem (see Sec. II C).

The similarity of the soliton phase diagrams for the static and dynamically periodic system in the presence of the Kerr non-linearity implies that including magnon-magnon interactions will modify the phase diagram of the Floquet system in the same way as it affects the spatially periodic one in Fig. 2.

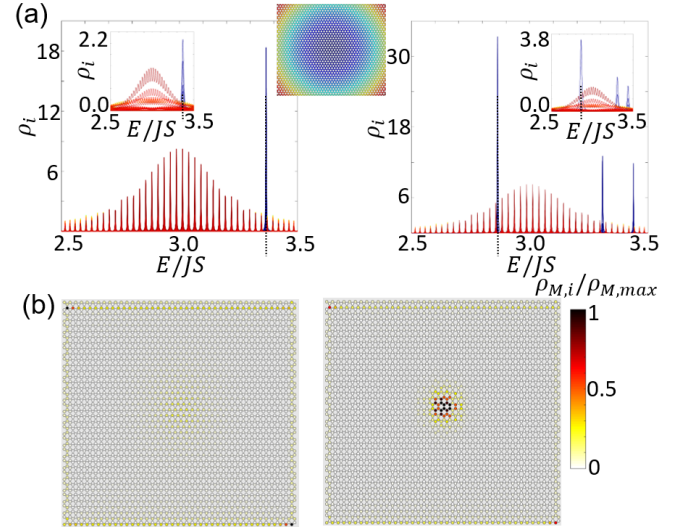


FIG. 4. (a) Density of state $\rho_i(E)$ at each site i for E inside the band gap with Lorentzian broadening $\epsilon = 10^{-3}(10^{-2})JS$ in the main (inserted) panels. The curves for all sites i are plotted over each other colorcoded according to the middle panel, i.e. line color is blue (red) for the sites in the center (edges). Left panel: soliton in region 1 of Fig. 1(c) ($K = -1$ and $P_0 = 11.5$); Right panel: soliton in region 2 of Fig. 1(c) ($K = -1$ and $P_0 = 12.9$). The black dashed lines indicate the respective soliton energies. (b) $\rho_{M,i} = \max \rho_i(E)$. Left panel: soliton in region 1 of Fig. 1(c) ($K = -1$ and $P_0 = 11.5$); Right panel: soliton in region 2 of Fig. 1(c) ($K = -1$ and $P_0 = 12.9$).

IV. EXPERIMENTAL REALIZATION

In the following we discuss the possibility of experimental realization of magnonic solitons in topologically nontrivial lattices including their edges. We realize that this is a larger order for the present stage of material science, since the number of potential systems is limited and the required structures might be difficult to fabricate. The real bottleneck could be the dissipation and heating, which has been completely disregarded in the theory. In order to keep these in check in excited systems, the materials and structures must be grown and fabricated with high magnetic quality.

The magnonic solitons discussed here exist in a lattice that is strongly and locally excited and has a topologically nontrivial band structure. Suggested realizations are artificial magnonic crystals on the $\gtrsim 100$ nm scale²⁰, but also natural materials such as the Kagome lattice of $\text{Lu}_2\text{V}_2\text{O}_7$ ³⁰ or the hexagonal lattice of CrBr_3 ^{31,32,69,70}. In magnetic films, solitons can be generated by spin-Hall oscillators^{53,71,72} in which a point contact of few tens of nanometer is deposited on top of a ferromagnet (e.g. permalloy)/heavy metal (e.g. Pt) bilayer. The associ-

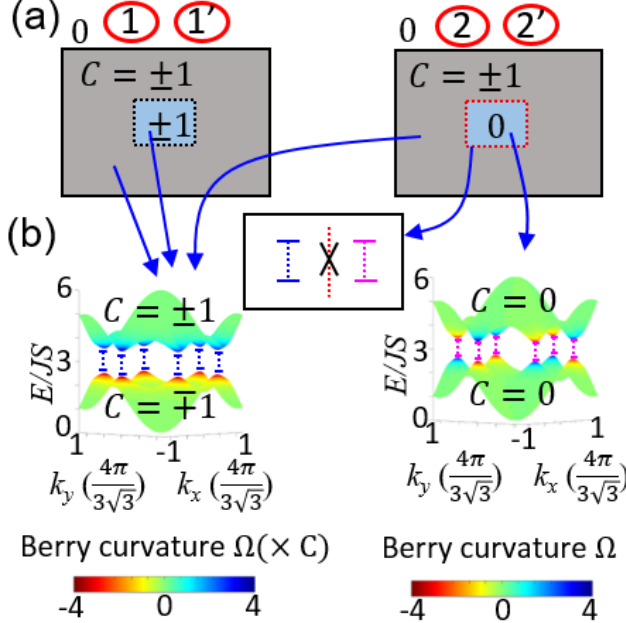


FIG. 5. (a) The topology of solitons on the Haldane lattice below and above $P_{u,c}$. The blue region is the soliton core that at high intensities may have a different Chern number C from the rest of the lattice (embedded into a medium with $C = 0$). (b) The bulk dispersion of the spin lattice for a nontrivial ($D = 0.01$ and $M = 0$) gap (left) and a trivial ($D = 0$ and $M = 3\sqrt{3} \times S/100$) gap (right). The color map encodes the Berry curvature $\vec{\Omega}(\vec{k}) = \Omega(\vec{k})\hat{z}$, for each band. The arrows indicate the connection of different phases in (a) to the relevant band structure panels in (b).

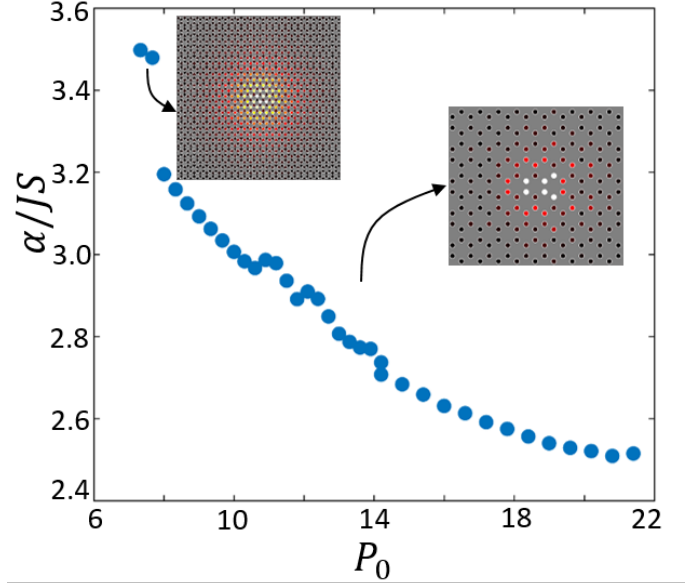


FIG. 6. The quasi-energy α (normalized by JS) of a soliton in a Floquet lattice with $K = -1$ as a function of P_0 . Two exemplary intensity distributions also depicted.

ated spin-orbit torques cause self-limited spatially localized large-angle precessional states referred to as “spin-wave bullets” (SWB)^{51,53,54} with frequency and amplitude controlled by the external magnetic field and charge current. In addition, precession can be phase-locked to an ac modulated charge current drive⁷².

Figure 7(a) sketches a device that could test our predictions. Two triangular contacts of high-mobility metal film (e.g. from Au) force a focused charge current $\vec{j}_{sb}(t)$ through the Pt, generating a SWB with frequency $E_s/(2\pi\hbar)$ in the permalloy film by the spin Hall effect. The latter is grown on a lattice of magnetic islands deposited in the holes of another magnetic material²⁰. The SWB generates dynamic dipolar and exchange fields that excite the underlying lattice. The existence and shape of the created lattice soliton can be studied using spatiotemporal Brillouin-light scattering measurement technique^{53,55,73,74} at resolutions down to ~ 50 nm^{53,73}. We give some estimates for this scenario in Appendix D. We can operate the device also without the Py layer. Current-induced self oscillations in the perpendicular magnetized material then require an in-plane field⁷⁵, but once excited, they can be sustained by an ac current in Pt without the field.

Other interesting systems are 2D van der Waals materials such as FePS_3 , $\text{Cr}_2\text{Ge}_2\text{Te}_6$, and transition metal trihalides, which have attracted attention for their tunable magnetic properties^{76–78}. In the latter, the transition metal (magnetic) sites form a hexagonal lattice, with a Heisenberg (super)exchange interaction mediated by the halides. In addition, the magnetic anisotropy can be tuned from in-plane to out-of plane by controlling

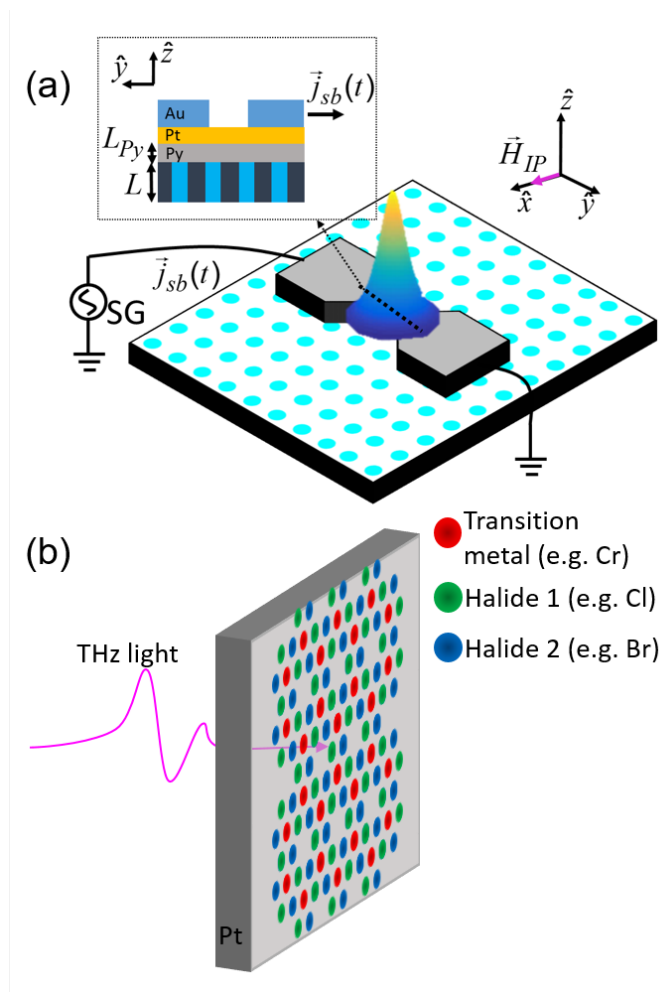


FIG. 7. (a) The schematic for an experimental realization of solitons described in this paper. SG stands for signal generator. The current $\vec{j}_{sb}(t)$ passes through a current line with a constricted region. A “spin-wave bullet (SWB)” wave function is shown schematically. The inset is a xz cross section, in which the materials of the SWB generation part (Au, Py, and Pt), as well as thickness of Py (L_{Py}) and lattice (L) are pointed out. The cyan color in both 3D and cross section panel indicate a magnetic pillar array embedded in another magnetic host²⁰. (b) Soliton generation in a 2D transition metal halide proximate to a heavy metal (e.g. Pt). A THz laser pulse irradiates the bilayer. The THz light excites magnons in the 2D material.

the halide composition: the magnetic anisotropy K of $\text{CrCl}_{3-x}\text{Br}_x$ varies linearly with x and changes from in-plane to out-of plane at $x \approx 2/9$. A DMI can be induced at the interface to a heavy metal like Pt. The magnetic states can be studied by X-ray magnetic circular dichroism (XMCD) spectroscopy with $\sim \text{nm}$ ($\sim 50 \text{ fs}$) spatial (temporal) resolution^{80,81}. The magnon gap width of MX_3 is in the range of 10 meV ⁸², i.e. we require THz excitation for an efficient excitation of the spin system. Topological solitons can then be generated in a monolayer of $\text{CrCl}_{3-x}\text{Br}_x$ on top of a heavy metal irradiated

by focused THz light with power above a certain threshold, as sketched in Fig. 7(b).

V. CONCLUSIONS

In conclusion, we discuss the existence and characteristics of soliton excitations in topologically nontrivial spin/magnonic lattices. We calculate the soliton formation phase diagram in the presence of crystalline anisotropies and magnon-magnon interactions. We understood in Sec. II C that without change in the topology of the underlying lattice, topologically distinct solitons can form. We classify the phase diagrams and predict a topological transition between soliton phases. Under certain conditions we find a phase separation in the soliton itself. This implies the existence of phase boundaries between solitons with trivial and non-trivial topological properties. The boundary separates non-linear excited states with trivial and non-trivial magnon gaps, which implies that at the boundary the spin gap vanishes. Our toolbox to date does not allow to study the physical consequences of such a topological interface for non-equilibrium systems, but judging from the impact of the discovery of the interface states of electronic topological insulators¹, we expect interesting physics.

Such interplay of nonlinearity, dynamics, and topology has very recently gained attention but is still widely unexplored^{64,83,84}. Unfortunately, experimental demonstration of a topologically nontrivial band gap of a magnonic lattice is still lacking. Magnonic and other Bosonic edge states are not thermally excited at low temperatures, which makes experimental observations challenging. Non-linearities in highly excited systems can overcome this problem^{35–38}. A soliton is a non-dispersive mode and its formation is a threshold process. Finding our predicted phase boundaries with sharp changes in soliton energies would be strong evidence of a nontrivial topology of the underlying lattice. In addition, the solitons phase texture as explained in Appendix B reveals information about the topology of the underlying lattice and the class of the soliton based on our classification. Solitons might serve for information storage and transfer, and interaction/collision between solitons as well as robust topological dynamic distinction, can be an information resource. The possible unidirectional motion of the soliton when generated at lattice edges³⁷ can lead to magnon squeezing⁸⁵ and enhanced optomagnonic coupling to photons⁸⁶. We suggest that the theoretical ideas can be realized and predictions tested in artificial magnonic lattices as well as hybrid structures with single layer van der Waals ferromagnets.

ACKNOWLEDGMENTS

M. Elyasi was supported by Postdoctoral Fellowship of Japan Society for the Promotion of Science (JSPS) for

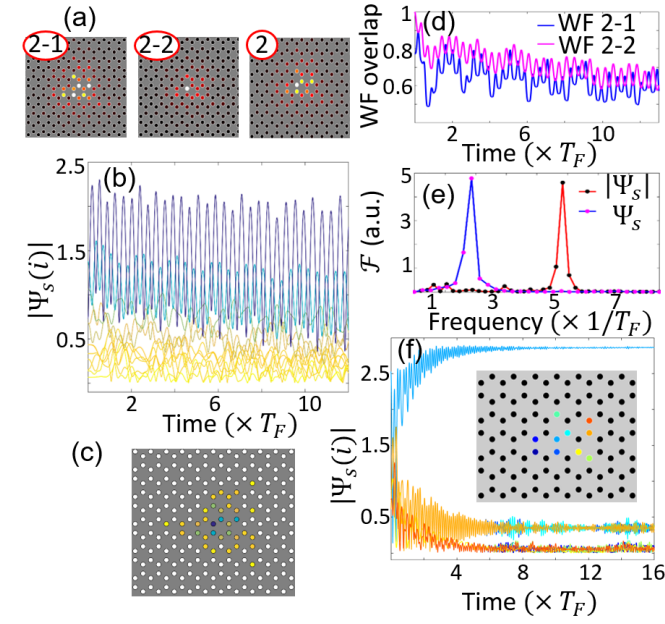


FIG. 8. Soliton breathing modes. (a) Two soliton WF's that are mean field solutions of each other's potential, labeled 2-1 and 2-2. The converged stationary WF found with an auxiliary Floquet potential as described in the text is labeled 2 (see also Fig. 1(c)). (b) The time-dependent soliton WF $|\Psi_s(i)|$, for sites i with significant participation in the WF. The curves for the presented sites are color coded in (c). The initial WF is the one corresponding to the 2-2 in (a). The results are for $K = -1$ and $P_0 = 16$, and $E_{2-1(2)}$ in $T_F = 2\pi/|E_{2-1} - E_{2-2}|$ is energy of 2-1(2-2) in (a). (c) The color code of the sites presented in (b). (d) The temporal evolution of the soliton WF overlap with the WF's corresponding to 2-1 and 2-2. (e) The effective amplitude of the Fourier transform of the WF and its amplitude. (f) Similar to (b) but for coarser time steps. The inset shows the color coding of the sites.

overseas researchers.

Appendix A: Floquet calculation methods

As explained briefly in Sec. II B, in regions 2 and 2' of parameter space the iterative solution scheme sometimes fails to converge, but oscillates between two (or more) states. This means that the eigenfunction of the (mean-field) nonlinear potential induced by one soliton is another soliton with different energy and vice versa, which indicates a breathing mode. Figure 8(a) shows example WF's of such a breathing mode, labeled as 2-1 and 2-2. Adopting a time-periodic (Floquet) potential that oscillates between the two solutions of 2-1 and 2-2 with natural period $T_F = 2\pi/|E_{2-1} - E_{2-2}|$ leads to a converged time-independent solution as shown in Fig. 8(a) with label 2. In the following, we discuss the rationale for T_F and the method to solve the corresponding Floquet problem.

Figure 8(b) shows the temporal evolution of the initial WF labeled by 2-1, for several neighboring sites (with colors explained in Fig. 8(c)). The WF amplitude $|\Psi_s|$ reflects the oscillation of the nonlinear potential, which for the anisotropy term is $K|\Psi_s|^2$. The normalized overlap of the 2-1 and 2-2 WF's in Fig. 8(d) reveals an out-of phase oscillation with fixed frequencies that appears to be a mixture of these two WF's. We test the assertion that $T_F = 2\pi\hbar/|E_{2-1} - E_{2-2}|$ by plotting $\mathcal{F}_{1(2)} = \sqrt{\sum_i |\mathcal{G}_{1(2)}(f)|^2}$ in Figure 8(e), where the sum is over the sites of the lattice and f is the frequency. $\mathcal{G}_{1(2)}(f)$ is the Fourier transform of $\Psi_s - \bar{M}_1$ ($|\Psi_s| - \bar{M}_2$), where $\bar{M}_{1(2)}$ is the time average of Ψ_s ($|\Psi_s|$). The frequency of the main oscillatory features are above $1/T_F$, supporting the assumption.

The time dependence for a coarser time steps is shown in Fig. 8(f). It can be seen, that the WF amplitude converges to a fixed point with energy below the bottom of the band; therefore the time steps chosen for evolution should be fine enough for convergence to the solitons inside the finite gap.

We now posit that a periodic potential in time with periodicity T_F can bridge the “breathing” and help finding a converged static WF. $U(T_F) = \mathcal{T} \exp\left(-i \int_0^{T_F} H_p(t) dt\right)$ is the evolution operator for time T_F under a periodic Hamiltonian $H_p(t)$ and \mathcal{T} is the time ordering operator. In the following we transform $U(T_F)$ into $e^{-iH_{p,eff}T_F}$, where $H_{p,eff}$ is a static Hamiltonian. The band structure of the system is then governed by $H_{p,eff}$ for integer multiples of T_F with eigenvalues or quasi-energies α . This is then a static equivalent of the Floquet H_p with energy band structure $E = \alpha$.

The Floquet Hamiltonian can be written in terms of its discrete Fourier components as $H_p(t) = \sum_{n=-\infty}^{\infty} H_p^{(n)} e^{in\omega_{pt}t}$, where $\omega_{pt} = 2\pi/T_F$ and $H_p^{(n)} = \int_0^{T_F} H_p(t) e^{-in\omega_{pt}t} dt / T_F$. The effective static Hamiltonian, $H_{p,eff}$, can then be written as a perturbation expansion²⁷

$$H_{p,eff} = H_{p,eff}^{(1)} + H_{p,eff}^{(2)} + H_{p,eff}^{(3)} + \dots, \quad (A1)$$

$$H_{p,eff}^{(1)} = H_p^{(0)}, H_{p,eff}^{(2)} = \frac{1}{2} \sum_{n \neq 0} \frac{[H_p^{(-n)}, H_p^{(n)}]}{n\omega_{pt}}, \quad (A2)$$

$$H_{p,eff}^{(3)} = \frac{1}{2} \sum_{n \neq 0} \frac{[[H_p^{(n)}, H_p^{(0)}], H_p^{(-n)}]}{n^2\omega_{pt}^2} + \frac{1}{3} \sum_{n', n \neq 0} \frac{[H_p^{(n)}, [H_p^{(n')}, H_p^{(-n-n')}]]}{n'n\omega_{pt}^2}. \quad (A3)$$

Higher order terms $H_{p,eff}^{(n>3)}$ can be disregarded for large enough ω_{pt} , as is the case in our calculations.

In the soliton search, we start with either 2-1 or 2-2 Floquet WF's at $t = 0$, $|\Psi_F(t = 0)\rangle$. Subsequently, we

evolve $|\Psi_F(t=0)\rangle$ using H_T for one period, T_F , using the split-step method by updating the non-linearities during the evolution. The resulting $|\Psi_F(0 \leq t \leq T_F)\rangle$ is only a Floquet WF when $|\Psi_F(0)\rangle = |\Psi_F(T_F)\rangle$. We diagonalize the resulting time-dependent Hamiltonian by choosing an appropriate cut-off for n in Eqs. (A1) to (A3). The WF with the largest overlap with $|\Psi_F(0)\rangle$ is chosen as the next $|\Psi_F(0)\rangle$ and the iteration goes on, until $|\Psi_F(t)\rangle$ becomes WF of the nonlinearity-induced time-periodic potential. In the calculations, we use n up to 50.

Panel 2 in Fig. 8(a) is the converged result of the described method for the initial breathing 2-1 and 2-2 WF's. The intensity distribution of 2 is a mixture of 2-1 and 2-2, as expected. After convergence the distribution and potentials are constant in time and the auxiliary periodic potential can be eliminated.

Appendix B: Soliton phase texture

We discuss now the soliton WF phase, $\Phi = \arg \Psi_s$ for the topological transition in Figs. 3 and 5(a-b). The spatial dependence of the local precession phase, plotted in Figs. 9(a-b) on a large scale around a soliton at the center, reveals a global phase texture of either three or six domains. The “order parameter” is here a phase wave vector \vec{k}_Φ defined as $\Phi \sim \text{mod}[\vec{k}_\Phi \cdot \vec{r} + \phi_0, 2\pi]$, where ϕ_0 is a constant.

A soliton in a material with topologically trivial band gap, such as an optical soliton with a vortex phase imprinted by the light shining on a photonic lattice, can only have a scalar phase⁸⁷. Its winding number is a measure in real space and since the lattice is topologically trivial, a non-zero value can only be imprinted by an external excitation. However, when the winding (Chern) number of the Berry (geometric) phase in momentum \vec{k} space⁶⁰ is nonzero, the real space domains are characterized by a vector \vec{k}_Φ .

For a given domain, we can measure \vec{k}_Φ by the angle θ_k

$$\theta_k = \sum_{\vec{k}} \text{mod} \left[\tan^{-1} \left(\frac{k_y}{k_x} \right), \pi \right] |\mathcal{G}_\Phi(\vec{k})|^2, \quad (\text{B1})$$

where $\mathcal{G}_\Phi(\vec{k})$ is the normalized discrete Fourier transform of the phase texture $\Phi(\vec{r}) = \arg \Psi_s(\vec{r})$. Here Ψ_s is a stationary solution with frequency $E_s/(2\pi\hbar)$. Both \vec{k}_Φ and $-\vec{k}_\Phi$, i.e. θ_k and $\theta_k + \pi$ should be included into the k-space summation, as demonstrated in Figs. 9(c-d), with colored points corresponding to the domains in Figs. 9(a-b).

From Figs. 3 and 5(a-b) and the corresponding discussion follows that for regions 1 and 1', the nontrivial ($C = \pm 1$) and a trivial ($C = 0$) topology meet at the edges to the vacuum, whereas in regions 2 and 2' a phase separation can exist within the soliton as well. Therefore, the phase texture of the solitons of region 1 and 1'

is solely determined by the outer edges, i.e. the minimal phase texture should contain three domains each with mean Fourier components deriving from two of the six Dirac points. The calculation of θ_k and $\theta_k + \pi$ using Eq. (B1) confirms this understanding as depicted in Fig. 9(c). For the solitons of region 2 and 2', both the inner and outer edges contribute to the phase texture. The inner edge is formed around the sites with $P_i > P_{u,c}$ (see Sec. II C), and its chirality is sketched by the yellow arrows in the inner panel of Fig. 9(d) for the WF corresponding to Fig. 9(b). We adopt arguments from Ref. [36] to determine the chirality of the inner edge. The phase texture of Fig. 9(b) reflects these two counter propagating edges by six domains, each with mean Fourier components occurring (approximately) at two of the six Dirac points,

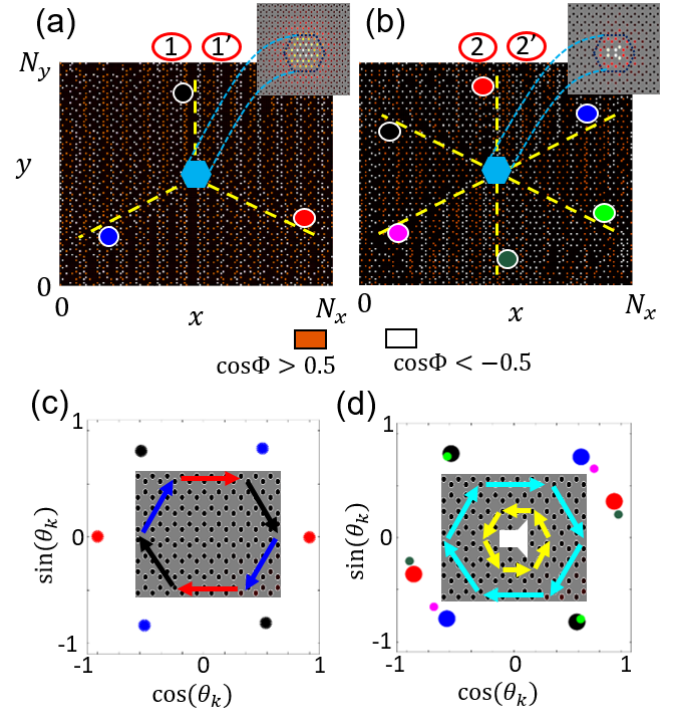


FIG. 9. (a) and (b): Spatially distributed $\cos \Phi$ of solitons centered at the origin (blue hexagon) from regions 1(1') and 2(2') in Figs. 1(c) and 2(a), respectively. For better visibility only sites with $\cos \Phi > 0.5$ and $\cos \Phi < -0.5$ are shown. The insets depict the intensity distribution close to the origin. The yellow dashed line separate the phase domains. The circles label each domain with colors that are the same as that of the dots in (c) and (d). (c) and (d): The dots indicate the calculated θ_k and $\theta_k + \pi$ (Eq. (B1)) of each domain in (a) and (b), respectively. The inner panels sketch the chirality of the gap modes in the real-space lattice by arrows. In (c), these have the same color as the corresponding θ_k and $\theta_k + \pi$. In (d), the chirality arrow of the outer (inner) edge is depicted by cyan (yellow). The inner edge is close to the origin of (b) where soliton intensity is maximized. Dots in (d) have a different sizes for clarity and the “loudspeaker” mimicks the soliton amplitude snapshot in (b),

as inferred from the values for θ_k and $\theta_k + \pi$ plotted in Fig. 9(d).

Appendix C: Floquet lattice

Eq. (10) is the Hamiltonian of a 2D-lattice of Heisenberg exchange-coupled local spins in the xy plane when illuminated by circularly polarized (CP) light with frequency ω . We show here that this is equivalent to a periodic static Haldane model.

A charge neutral particle with magnetic moment accumulates (Aharonov-Casher) phase when moving with respect to an electric field⁶⁸, analogous to the Aharonov-Bohm phase for charged particles moving with respect to magnetic fields⁸⁸. The accumulated phase upon hopping of a magnon, $A_{ij} = g\mu_B \int_{\vec{r}_i}^{\vec{r}_j} \vec{A}(t) \cdot d\vec{r}$ for $\vec{A}(t) = E_0(\pm \sin \omega t, \cos \omega t, 0)/\omega$, is $A_{ij} \propto g\mu_B E_0(\pm \cos(\omega t) \cos(\phi_{ij}) + \sin(\omega t) \sin(\phi_{ij}))/\omega$, where E_0 is the light electric field amplitude, g is the Landé g -factor, μ_B is Bohr magneton, and ϕ_{ij} is the angle of the vector connecting site i at \vec{r}_i to j at \vec{r}_j .

Using Eqs. (A1) to (A3), the Hamiltonian Eq. (10) can to leading order in the small parameter $\xi = g\mu_B E_0/\omega$ be transformed into a time-independent sum of two contributions

$$H_{F,eff}^{(1)} = J \sum_{\langle i,j \rangle} [S_i^z S_j^z + \mathcal{J}_0(\xi)(S_i^x S_j^x + S_i^y S_j^y)], \quad (C1)$$

$$H_{F,eff}^{(2)} = \sum_{\langle\langle i,j \rangle\rangle} \sum_{n \neq 0} \frac{(-1)^n J \mathcal{J}_n^2(\xi)}{n\omega} \sin(n \frac{2\pi}{3} v_{ij}) \vec{S}_k \cdot (\vec{S}_i \times \vec{S}_j), \quad (C2)$$

where k is a site between two next nearest neighbors (NNN) i and j , and \mathcal{J}_n is the n 'th order Bessel function of the first kind. Focussing on a perpendicular equilibrium magnetization, \vec{S}_k can be written as a sum of a static and dynamic contribution as $\vec{S}_k = S_{0,k} \hat{z} + \delta \vec{S}_k$ in Eq. (C2), which to leading order reduces to a term similar to the DMI in Eq. (1) with effective DMI coefficient $D_F = -\sqrt{3}JS\mathcal{J}_1^2(\xi)/\omega$,

$$H_{p,eff} = H_{F,eff}^{(1)} + \sum_{\langle\langle i,j \rangle\rangle} D_F v_{ij} \hat{z} \cdot (\vec{S}_i \times \vec{S}_j) \quad (C3)$$

where ξ and ω are tunable by the power and frequency of the light. We thereby recover the static Haldane model in the Floquet manner without intrinsically broken inversion symmetry (and therefore DMI). Non-linearities affect $H_{p,eff}$ in the same way as in the main text. Hence, the soliton search procedure as explained in Appendix A can be applied, whereby the Floquet period T_F in Appendix A is fixed by $T = 2\pi/\omega$. Moreover, the initial trial WF of the iterative method is $\langle \Psi_F(t=0) | n_i | \Psi_F(t=0) \rangle = P_0$ for a site $i = 0$ in the bulk and zero otherwise.

Appendix D: Parameter estimates

Magnons in crystals with periodic magnetization M_s on length scales of $d \sim 0.5 \mu\text{m}$ are dominated by dipolar interactions. In a structure consisting of a regular lattice of holes in a host magnet film that are filled with sufficiently different magnetic materials and a filling fraction $F \sim 10^{-2}$, the Chern number of a specific band can be tuned between zero, 1 and 2, by changing d and the aspect ratio of the unit cell²⁰. The total spin in each unit cell is then $S = (M_{s,f}F + M_{s,l})d^2L/(\gamma\hbar) \approx M_{s,l}d^2L/(\gamma\hbar)$, where $-\gamma$ is the gyromagnetic ratio and subscript l (f) refers to the magnetic material of the lattice host (filling). S can be tuned by the film thickness L , while the topological invariant is kept constant, as long as the translational invariance along \hat{z} is a good assumption (thick film limit). We assume that we can locally excite the lowest magnonic bands with constant amplitude along \hat{z} by the dynamic spin transfer torque of a spin wave bullet in a Py overlayer with in-plane magnetization, as in Figure 7(a).

Based on the typical frequencies of the band widths of dipolar magnonic lattices (corresponding to JS in the Haldane model) $\sim 10 \text{ GHz}$, for $L \sim 10 \mu\text{m}$, i.e. $S \sim 10^{15}$, we have a correspondence to $J \sim 0.0001$ in the Haldane model. The gap width and topology of the magnonic lattice is governed by the aspect ratio of the rectangular 2D unit cell with fixed area. It can be tuned to correspond to the D/J parameter used here. Therefore, the soliton phase diagram for $K = -1$ of Fig. 1(c) can be achieved in a magnonic lattice with $K \sim -0.001$ by a crystalline anisotropy constant K_u through $K = -2\gamma K_u/(\mu_0 M_{s,l}S)$, or $K_u \sim 10^4 \text{ J/m}^3$ for $\gamma = 2.2 \times 10^5 \text{ A/(m}\cdot\text{s)}$ and $M_{s,l} = 10^5 \text{ A/m}$. For comparison, K_u for YIG and L1₀ FePt, are of the order of $\sim 10^3$ and $\sim 10^6 \text{ J/m}^3$, respectively^{89,90}. Tuning S by changing L while keeping all other parameters intact, thus should allow resolving soliton phase diagrams with (Fig. 2) and without (Fig. 1(c)) magnon-magnon interactions. A possible concrete choice would be YIG for the film, while the filling material is Fe (or Co). An ability to change the crystalline anisotropy from say 10^3 to 10^4 J/m^3 by using different crystal growth directions, doping, or gating of YIG, could be useful to map the soliton phase diagrams.

The spin-Hall oscillators that generate self-localized oscillations (SWB) can be fabricated with spatial half-widths at half-maximum R_{SWB} of $\sim 500 \text{ nm}$ ⁵³, which would cover approximately a unit cell of the lattice in the previous example, which is sufficient to generate the localized solitons predicted in Figs. 1(c) and 2. In a $\sim 10 \mu\text{m}$ wide disk Py/Pt bilayer the SWB were excited for an in-plane equilibrium magnetization. For a fixed current above threshold, an in-plane magnetic field \vec{H}_{IP} of $4 \times 10^4 - 12 \times 10^4 \text{ A/m}$ can tune the SWB frequencies in the range of $5 - 10 \text{ GHz}$. The perpendicular magnetization of the underlying magnonic lattice is not significantly affected when the perpendicular anisotropy is strong enough, e.g. $K_u \sim 10^4 \text{ J/m}^3$ while the in-plane

magnetization of Py is stabilized by the thin film shape anisotropy.

Modeling the SWB by a macrospin precession within the bullet volume, we can calculate the effective dipolar field on the lattice below the SWB as $h_{SWB,l} > \pi R_{SWB}^2 L_{Py} M_{s,Py} \sin \theta_c / (r_w^2 L)$, where L_{Py} is the Py layer thickness (5 nm), $M_{s,Py} = 7 \times 10^5$ A/m. θ_c is the precession cone angle, and $2r_w$ is the diameter of the expected lattice soliton. With $r_w \approx 0.1 \mu\text{m}$, $\theta_c = \pi/4$, $h_{SWB,l} > 2.5 \times 10^3$ A/m. A magnon mode in the lattice resonant with the frequency ω_{SWB} of the driving field $h_{SWB,l}$ is

estimated as $n_l \sim (2h_{SWB,l} \gamma^2 R_{SWB}^2 L \sqrt{M_{s,l} / 2\gamma \hbar} / \zeta_m)^2$, where ζ_m is the magnetic damping, which in a best case scenario ~ 1 MHz for YIG. Therefore, $n_l \sim 1.5 \times 10^{15}$, which is $\sim 1 - 10 S$ that is in the range of P_0/S of Figs. 1(c) and 2. By adopting M_s of the host material YIG (which is smaller than the filling materials Fe or Co), this is a lower bound for n_l . It should be noted that $h_{SWB,l}$ and consequently n_l can be tuned by the charge current amplitude and the locking microwave charge current power⁷². In the steady state the charge current generates an SWB that stabilizes the solitons by regenerating the losses due to damping. \vec{E}

-
- ¹ M. Z. Hasan and C. L. Kane, Rev. Mod. Phys. **82**, 3045 (2010).
 - ² X.-L. Qi and S.-C. Zhang, Rev. Mod. Phys. **83**, 1057 (2011).
 - ³ C. Nayak, S. H. Simon, A. Stern, M. Freedman, and S. D. Sarma, Rev. Mod. Phys. **80**, 1083 (2008).
 - ⁴ K. v. Klitzing, G. Dorda, and M. Pepper, Phys. Rev. Lett. **45**, 494 (1980).
 - ⁵ F. D. M. Haldane, Phys. Rev. Lett. **61**, 2015 (1988).
 - ⁶ C. L. Kane and E. J. Mele, Phys. Rev. Lett. **95**, 226801 (2005).
 - ⁷ N. Regnault and B. A. Bernevig, Phys. Rev. X **1**, 021014 (2011).
 - ⁸ B. A. Bernevig and F. D. M. Haldane, Phys. Rev. Lett. **100**, 246802 (2008).
 - ⁹ R. B. Laughlin, Phys. Rev. Lett. **50**, 1395 (1983).
 - ¹⁰ B. A. Bernevig, T. L. Hughes, and S. C. Zhang, 2006, Science **314**, 1757 (2006).
 - ¹¹ H. Zhang, C.-X. Liu, X.-L. Qi, X. Dai, Z. Fang, and S.-C. Zhang, 2009, Nature Phys. **5**, 438 (2009).
 - ¹² L. Fu and C. L. Kane, 2007, Phys. Rev. B **76**, 045302 (2007).
 - ¹³ P. A. Lee, N. Nagaosa, and X. G. Wen, Rev. Mod. Phys. **78**, 17 (2006).
 - ¹⁴ L. Balents, Nature (London) **464**, **199** (2010).
 - ¹⁵ S. Yan, D. A. Huse, and S. R. White, Science **332**, 1173 (2011).
 - ¹⁶ L. Cincio and G. Vidal, Phys. Rev. Lett. **110**, 067208 (2013).
 - ¹⁷ M. König, S. Wiedmann, C. Brune, A. Roth, H. Buhmann, L. W. Molenkamp, X.-L. Qi, and S.-C. Zhang, Science **318**, 766 (2007).
 - ¹⁸ F. D. M. Haldane and S. Raghu, Phys. Rev. Lett. **100**, 013904 (2008).
A. B. Khanikaev, S. H. Mousavi, W.-K. Tse, M. Kargarian, A. H. MacDonald, and G. Shvets, Nat. Mater. **12**, 233 (2013).
 - ¹⁹ Z. Yang, F. Gao, X. Shi, X. Lin, Z. Gao, Y. Chong, and B. Zhang, Phys. Rev. Lett. **114**, 114301 (2015).
 - ²⁰ R. Shindou, R. Matsumoto, S. Murakami, and J.-I. Ohe, Phys. Rev. B **87**, 174427 (2013).
R. Shindou, J.-I. Ohe, R. Matsumoto, S. Murakami, and E. Saitoh, Phys. Rev. B **87**, 174402 (2013).
 - ²¹ L. Fu and C. L. Kane, Phys. Rev. Lett. **102**, 216403 (2009).
 - ²² R. W. Damon, and J. R. Eschbach, J. Phys. Chem. Solids **19**, 308 (1961).
 - ²³ D. D. Stancil and A. Prabhakar, Spin waves, Springer (2009).
 - ²⁴ Y. Onose, T. Ideue, H. Katsura, Y. Shiomi, N. Nagaosa, and Y. Tokura, Science **329**, 297 (2010).
 - ²⁵ R. Matsumoto and S. Murakami, Phys. Rev. Lett. **106**, 197202 (2011).
 - ²⁶ J. H. Shirley, Phys. Rev. **138**, B979 (1965).
 - ²⁷ I. Scholz, J. D. van Beek, and M. Ernst, Solid State Nucl. Magn. Reson. **37**, 39 (2010).
 - ²⁸ T. Kitagawa, E. Berg, M. Rudner, and E. Demler, Phys. Rev. B **82**, 235114 (2010).
 - ²⁹ L. Zhang, J. Ren, J.-S. Wang, and B. Li, Phys. Rev. B **87**, 144101 (2013).
 - ³⁰ A. Mook, J. Henk, and I. Mertig, Phys. Rev. B **91**, 224411 (2015).
 - ³¹ S. K. Kim, H. Ochoa, R. Zarzuela, and Y. Tserkovnyak, Phys. Rev. Lett. **117**, 227201 (2016).
 - ³² S. A. Owerre, J. Phys.: Condens. Matter. **28**, 386001 (2016).
 - ³³ S. A. Owerre, J. Phys. Comm. **1**, 021002 (2017).
 - ³⁴ M. C. Rechtsman, J. M. Zeuner, Y. Plotnik, Y. Lumer, D. Podolsky, F. Dreisow, S. Nolte, M. Segev, and A. Szameit, Nature (London) **496**, 196 (2013).
 - ³⁵ B. Galilo, D. K. K. Lee, and R. Barnett, Phys. Rev. Lett. **115**, 245302 (2015).
 - ³⁶ Y. Lumer, Y. Plotnik, M. C. Rechtsman, and M. Segev, Phys. Rev. Lett. **111**, 243905 (2013).
 - ³⁷ D. Leykam and Y. D. Chong, Phys. Rev. Lett. **117**, 143901 (2016).
 - ³⁸ M. J. Ablowitz, C. W. Curtis, and Y.-P. Ma, Phys. Rev. A **90**, 023813 (2014).
 - ³⁹ A. M. Kosevich, B. A. Ivanov, and A. S. Kovalev, Phys. Rep. **194**, 117 (1990).
 - ⁴⁰ O. Zobay, S. Potting, P. Meystre, and E. M. Wright, Phys. Rev. A **59**, 643 (1999).
 - ⁴¹ A. Trombettoni and A. Smerzi, Phys. Rev. Lett. **86**, 2353 (2001).
 - ⁴² P. J. Y. Louis, E. A. Ostrovskaya, C. M. Savage, and Y. S. Kivshar, Phys. Rev. A **67**, 013602 (2003).
 - ⁴³ B. Eiermann, T. Anker, M. Albiez, M. Taglieber, P. Treutlein, K.-P. Marzlin, and M. K. Oberthaler, Phys. Rev. Lett. **92**, 230401 (2004).
 - ⁴⁴ P. D. Drummond, R. M. Shelby, S. R. Friberg, and Y. Yamamoto, Nature **365**, 307 (1993).
 - ⁴⁵ M. Mitchell, M. Segev, T. H. Coskun, and D. N. Christodoulides, Phys. Rev. Lett. **79**, 4990 (1997).

- ⁴⁶ G. I. Stegeman, and M. Segev, *Science* **286**, 1518 (1999).
- ⁴⁷ X. Wang, Z. Chen, J. Wang, and J. Yang, *Phys. Rev. Lett.* **99**, 243901 (2007).
- ⁴⁸ A. N. Slavin and I. V. Rojdestvenski, *IEEE Trans. Magn.* **30**, 37 (1994).
- ⁴⁹ O. Buttner, M. Bauer, S. O. Demokritov, B. Hillebrands, Y. S. Kivshar, V. Grimalsky, Y. Rapoport, T. Shevchenko, M. P. Kostylev, B. A. Kalinikos, and A. N. Slavin, *J. Appl. Phys.* **87**, 5088 (2000).
- ⁵⁰ M. Wu, B. A. Kalinikos, L. D. Carr, and C. E. Patton, *Phys. Rev. Lett.* **96**, 187202 (2006).
- ⁵¹ S. Kaka, M. R. Pufall, W. H. Rippard, T. J. Silva, S. E. Russek, and J. A. Katine, *Nature* **437**, 389 (2005).
- ⁵² A. Slavin and V. Tiberkevich, *IEEE Trans. Magn.* **45**, 1875 (2009).
- ⁵³ V. E. Demidov, S. Urazhdin, H. Ulrichs, V. Tiberkevich, A. Slavin, D. Baither, G. Schmitz, and S. O. Demokritov, *Nature Mater.* **11**, 1028 (2012).
- ⁵⁴ A. Slavin and V. Tiberkevich, *Phys. Rev. Lett.* **95**, 237201 (2005).
- ⁵⁵ V. E. Demidov, O. Dzyapko, S. O. Demokritov, G. A. Melkov, and A. N. Slavin, *Phys. Rev. Lett.* **100**, 047205 (2008).
- ⁵⁶ S. M. Rezende, *Phys. Rev. B* **81**, 020414 (2010).
- ⁵⁷ B. A. Malomed, O. Dzyapko, V. E. Demidov, and S. O. Demokritov, *Phys. Rev. B* **81**, 024418 (2010).
- ⁵⁸ I. Dzyaloshinskii, *Phys. Chem. Solids* **4**, 241 (1958).
- ⁵⁹ T. Moriya, *Phys. Rev.* **120**, 91 (1960).
- ⁶⁰ D. Xiao, M.-C. Chang, and Q. Niu, *Rev. Mod. Phys.* **82**, 1959 (2010).
- ⁶¹ D. N. Christodoulides and R. I. Joseph, *Opt. Lett.* **13**, 794 (1988).
- ⁶² Y. S. Kivshar, *Opt. Lett.* **18**, 1147 (1993).
- ⁶³ W. P. Su, J. R. Schrieffer, and A. J. Heeger, *Phys. Rev. B* **22**, 2099 (1980).
- ⁶⁴ Y. Hadad, A. B. Khanikaev, and Andrea Alu, *Phys. Rev. B* **93**, 155112 (2016).
- ⁶⁵ O. Cohen, T. Schwartz, J. W. Fleischer, M. Segev, D. N. Christodoulides, *Phys. Rev. Lett.* **91**, 113901 (2003).
- ⁶⁶ A. Mesaros, S. Papanikolaou, C. F. J. Flipse, D. Sadri, and J. Zaanen, *Phys. Rev. B* **82**, 205119 (2010).
- ⁶⁷ D. Xiao, W. Yao, and Q. Niu, *Phys. Rev. Lett.* **99**, 236809 (2007).
- ⁶⁸ Y. Aharonov and A. Casher, *Phys. Rev. Lett.* **53**, 319 (1984).
- ⁶⁹ T. Ideue, Y. Onose, H. Katsura, Y. Shiomi, S. Ishiwata, N. Nagaosa, and Y. Tokura, *Phys. Rev. B* **85**, 134411 (2012).
- ⁷⁰ L. J. D. Jongh and A. R. Miedema, *Adv. Phys.* **50**, 947 (2001).
- ⁷¹ L. Liu, C.-F. Pai, D. C. Ralph, and R. A. Buhrman, *Phys. Rev. Lett.* **109**, 186602 (2012).
- ⁷² V. E. Demidov, H. Ulrichs, S. V. Gurevich, S. O. Demokritov, V. S. Tiberkevich, A. N. Slavin, A. Zholud, and S. Urazhdin, *Nat. Commun.* **5**, 3179 (2014).
- ⁷³ S. O. Demokritov and V. E. Demidov, *IEEE Trans. Mag.* **44**, 6 (2008).
- ⁷⁴ D. A. Bozhko, A. A. Serga, P. Clausen, V. I. Vasyuchka, F. Heussner, G. A. Melkov, A. Pomyalov, V. S. Lvov, and B. Hillebrands, *Nat. Phys.* **12**, 1057 (2016).
- ⁷⁵ B. Divinskiy, V. E. Demidov, A. Kozhanov, A. B. Rinkevich, S. O. Demokritov, and S. Urazhdin, *Appl. Phys. Lett.* **111**, 032405 (2017).
- ⁷⁶ K. S. Burch, D. Mandrus, and J.-G. Park, *Nature* **563**, 47 (2018).
- ⁷⁷ B. Huang, G. Clark, D. R. Klein, D. MacNeill, E. Navarro-Moratalla, K. L. Seyler, N. Wilson, M. A. McGuire, D. H. Cobden, D. Xiao, W. Yao, P. Jarillo-Herrero, and X. Xu, *Nat. Nanotechnol.* **13**, 544 (2018).
- ⁷⁸ B. Huang, G. Clark, E. Navarro-Moratalla, D. R. Klein, R. Cheng, K. L. Seyler, D. Zhong, E. Schmidgall, M. A. McGuire, D. H. Cobden, W. Yao, D. Xiao, P. Jarillo-Herrero, and X. Xu, *Nature* **546**, 270 (2017).
- ⁷⁹ M. Abramchuk, S. Jaszewski, K. R. Metz, G. B. Osterhoudt, Y. Wang, K. S. Burch, and F. Tafti, *Adv. Mater.* **30**, 1801325 (2018).
- ⁸⁰ G. Schutz, M. Knälle, and H. Ebert, *Phys. Scr.* **1993**, 302 (1993).
- ⁸¹ O. Kfir, P. Grychtol, E. Turgut, R. Knut, D. Zusin, D. Popmintchev, T. Popmintchev, H. Nembach, J. M. Shaw, A. Fleischer, H. Kapteyn, M. Murnane, and O. Cohen, *Nat. Photon.* **9**, 99 (2015).
- ⁸² D. R. Klein, D. MacNeill, J. L. Lado, D. Soriano, E. Navarro-Moratalla, K. Watanabe, T. Taniguchi, S. Manni, P. Canfield, J. Fernández-Rossier, P. Jarillo-Herrero, *Science* **360**, 1218 (2018).
- ⁸³ G. Engelhardt, M. Benito, G. Platero, and T. Brande, *Phys. Rev. Lett.* **117**, 045302 (2016).
- ⁸⁴ V. Peano, M. Houde, C. Brendel, F. Marquardt, and A. A. Clerk, *Nat. Commun.* **7**, 10779 (2016).
- ⁸⁵ M. Kostylev, A. B. Ustinov, A. V. Drozdovskii, B. A. Kalinikos, E. Ivanov, *arXiv:1811.02104* (2018)
- ⁸⁶ A. Osada, R. Hisatomi, A. Noguchi, Y. Tabuchi, R. Yamazaki, K. Usami, M. Sadgrove, R. Yalla, M. Nomura, and Y. Nakamura, *Phys. Rev. Lett.* **116**, 223601 (2016).
- ⁸⁷ X. Zhang, N. Zhu, C.-L. Zou, and H. X. Tang, *Phys. Rev. Lett.* **117**, 123605 (2016).
- ⁸⁸ J. A. Haigh, A. Nunnenkamp, A. J. Ramsay, and A. J. Ferguson, *Phys. Rev. Lett.* **117**, 133602 (2016).
- ⁸⁹ S. Sharma, Y. M. Blanter, and G. E. W. Bauer, *Phys. Rev. B* **96**, 094412 (2017).
- ⁹⁰ D. N. Neshev, T. J. Alexander, E. A. Ostrovskaya, Y. S. Kivshar, H. Martin, I. Makasyuk, and Z. Chen, *Phys. Rev. Lett.* **92**, 123903 (2004).
- ⁹¹ Y. Aharonov and D. Bohm, *Phys. Rev. B* **115**, 485 (1959).
- ⁹² J.-U. Thiele, L. Folks, M. F. Toney, and D. K. Weller, *J. Appl. Phys.* **84**, 5686 (1998).
- ⁹³ P. H. Bryant, C. D. Jeffries, and K. Nakamura, *Phys. Rev. A* **38**, 4223 (1988).